The three-dimensional structure of halorhodopsin to 5 Å by electron crystallography: A new unbending procedure for two-dimensional crystals by using a global reference structure

Edmund R. S. Kunji*, Susanne von Gronau†, Dieter Oesterhelt†, and Richard Henderson*‡

*MRC Laboratory of Molecular Biology, Hills Road, CB2 2QH Cambridge, England, and †Max-Planck-Institut für Biochemie, W-82152 Martinsried, Germany

Contributed by Richard Henderson, February 14, 2000

Electron microscopy does not, in principle, require highly ordered crystals to determine a high-resolution structure. Nevertheless, crystals of any type help to constrain the molecules into a more limited range of orientations and positions, from which it is easier to carry out structure determination. We describe an improved procedure for determination of crystalline disorder, which we have applied to poorly ordered two-dimensional crystals of the chloride pump halorhodopsin from *Halobacterium salinarum*. The new image analysis procedure involves the use of a reference projection calculated from a global three-dimensional map to carry out the initial cross-correlation analysis. Coupled with a greater number of images taken with field emission gun microscopes, this has allowed us to calculate a three-dimensional structure for halorhodopsin, in which the seven transmembrane helices and certain molecular features, such as the β-ionone ring of retinal, are now resolved.

Halorhodopsin (hR) is a light-driven chloride pump in the plasma membrane of halophilic archeons that belongs to the archeal rhodopsin family, which, in addition, consists of bacteriorhodopsin (bR) and two receptors, sensory rhodopsin I (sRI) and II (sRII). The best studied member of this family is bR, which pumps protons out of the cell by light-induced all-trans to 13-cis isomerization of the retinal chromophore. The two sensory rhodopsins are phototaxis receptors that send light-induced signals to tightly bound transducer proteins (HtrI and HtrII), which in turn control a phosphorylation cascade modulating the cell's phototactic behavior through the flagellar motor (reviewed in refs. 1–3). Twenty-five primary sequences of archeal rhodopsins have been identified in different strains and genera of Halobacteriaceae (1). All members of the family are predicted to have seven transmembrane α-helices that form a pocket for the covalently attached chromophore retinal. Amino acid sequence alignments indicate that the overall identity is 20–35% between the four different rhodopsins with higher similarity within the bR-hR cluster and within the sRI-sRII cluster. In addition to a similar overall structure, hR and bR might also share a common transport mechanism, despite the fact that their ion translocations are in opposite directions. Several studies have shown that bR can bind halide ions and can be converted into an hR-like pump (4–7). On the other hand, hR can also function as a proton pump in the presence of azide (8–9).

Several high-resolution structures of bR have been published recently, determined either by electron or x-ray crystallography (reviewed in ref. 10). The only currently available three-dimensional (3D) structure for hR is a low-resolution 3D map derived from electron crystallographic analysis of two-dimensional (2D) crystals naturally produced in the hR-overproducing strain D2 (11, 12). These have a square lattice with unit cell dimensions of 102 Å and $p42_12$ symmetry, indicating that in the crystal half of the molecules, grouped in tetramers, are inserted upside down. Although the 7-Å structure of hR is similar to bR, the tilted helices were poorly resolved.

The hR crystals are relatively small as well as disordered and often contain holes. The crystals are too small for electron diffraction, and image amplitudes are decreased by crystal disorder. Previously, the translational component of these distortions was corrected by a procedure that uses as a reference initially a small part of, and later the average of, the whole crystal to unbend the image so that it closely approximates an image of a perfect crystal. However, this approach is limited by the quality of individual crystals. In this paper, we present an improved unbending procedure that uses the existing low-resolution structure (12) as reference. On average, 8% more spots with acceptable signal-to-noise ratio were obtained. The new procedure, together with 85 new images, has led to the improved 3D structure presented here. The overall phase residual now demonstrates some reliable phases to 4 Å, but because of limited sampling the effective resolution is nearer to 5 Å in the plane of the membrane and 12 Å perpendicular.

Materials and Methods

Sample Preparation and Electron Cryomicroscopy. High-density (1.18 g/ml) membranes were isolated from an hR-overproducing strain D2 of *Halobacterium salinarum* as described (11, 13). These membranes were variable in size, and only about one-third contained crystalline patches. To select the largest and most crystalline membrane patches, the membranes were subjected to differential centrifugation. The pellet obtained after 5 min of centrifugation at 50,000 × *g* showed an enrichment of larger membranes, but the average diameter of the crystalline patches, being in the range of 0.3 to 0.4 μm, was only slightly larger than reported previously (12). This fraction was used to prepare frozen hydrated samples. Briefly, membranes suspended in a drop were adsorbed to one side of 4-day-old carbon-coated electron microscope grids, blotted for 30 sec at 4°C and high humidity, and rapidly frozen by plunging into liquid ethane at −180°C. The grids were stored under liquid nitrogen.

The grids were transferred under liquid nitrogen to a Gatan 626 electron microscope cold stage and introduced into the 200-keV Hitachi HF2000 cold field emission gun (FEG) microscope or the liquid helium-cooled microscope at the Fritz Haber Institute in Berlin (Sophie) operated at 160 keV. The sample temperature was 100 K and 8 K approximately in each case.

Abbreviations: FEG, field emission gun; hR, halorhodopsin; bR, bacteriorhodopsin; 3D, three dimensional; 2D, two dimensional.

‡To whom reprint requests should be addressed. E-mail: rh15@mrc-lmb.cam.ac.uk.

The publication costs of this article were defrayed in part by page charge payment. This article must therefore be hereby marked "*advertisement*" in accordance with 18 U.S.C. §1734 solely to indicate this fact.

Article published online before print: *Proc. Natl. Acad. Sci. USA*, 10.1073/pnas.080064697. Article and publication date are at www.pnas.org/cgi/doi/10.1073/pnas.080064697

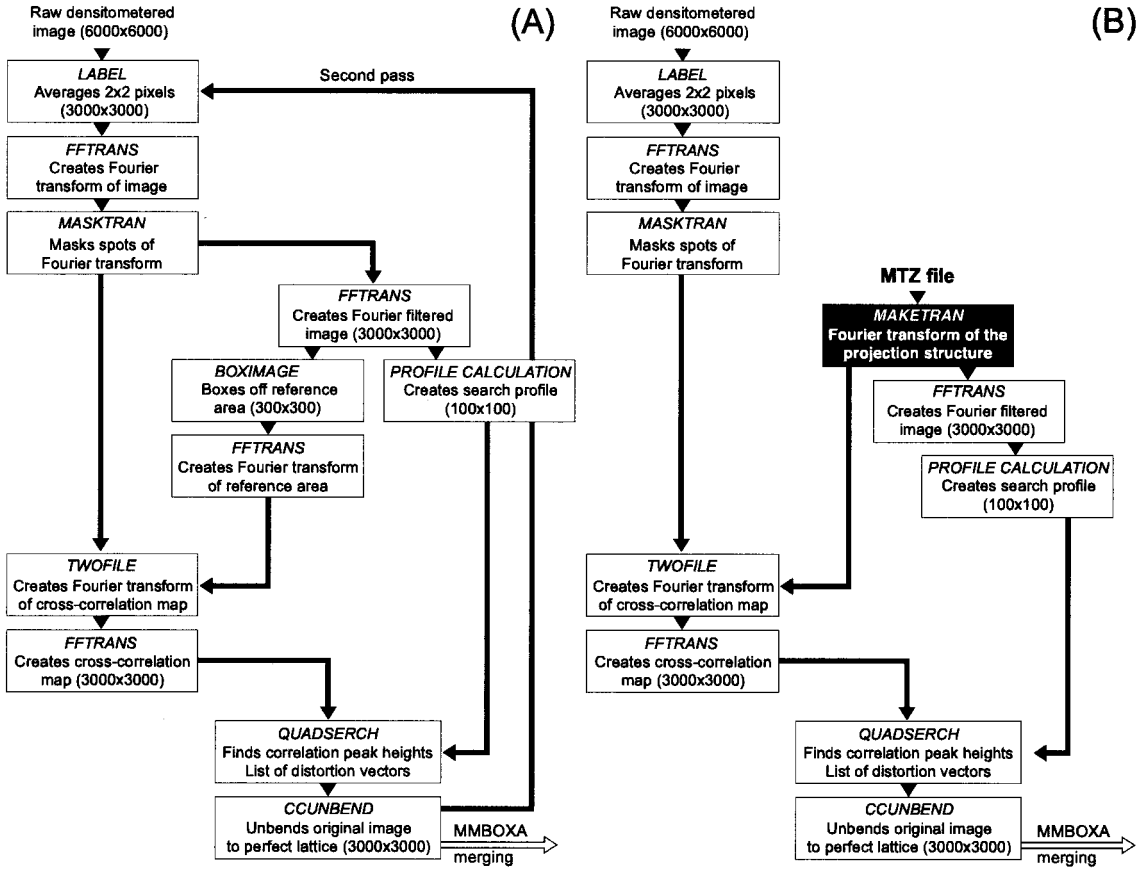

Fig. 1. Overview of the sequence of programs (15) used in the unbending procedure with the crystal (*A*) and the 3D density map (*B*) as reference for cross-correlation Fourier analysis.

Micrographs were recorded under standard low-dose conditions (10–15 $e^-/Å^2$) by using either a flood beam or a spotscan exposure procedure (14). The magnification was between 40,000 and 60,000, and the exposure times for flood beam images were between 0.5 and 2.0 sec; and for spotscan images 300 msec per spot, having an average diameter of 1 cm on the film. Images were recorded using an underfocus between 500 and 18,000 Å. A 50-μm C2 aperture was used for flood beam and a 30-μm C2 aperture for spotscan images. The majority of the pictures were taken by using a 10-μm objective aperture. The highest tilt angle of the specimen that could still be processed was 41°. The Kodak SO-163 films were developed in a D19 developer (12 min at 20°C).

Image Processing, Contrast Transfer Correction, and Data Merging. Micrographs that possessed good resolution in all directions were selected by optical diffraction and digitized by using a Zeiss-SCAI scanner with a 7-μm pixel size. The image processing followed earlier protocols (12) with the exception of the new cross-correlation step described below.

Part of the fading of image contrast at high resolution is caused by inherent disorder of the crystals. Previously, translational distortions of the crystal were corrected, termed unbending, by identifying the displacement of the unit cells compared with the ideal lattice by cross-correlation Fourier analysis by using a reference area from the center of the crystal itself. Here, we present an unbending procedure that uses the best current 3D map of the structure derived from all images so far included in the structure determination as a reference. In this case, we began with the previous low-resolution 3D map of hR (12). To facilitate a comparison between the two unbending procedures, the sequences of programs used are depicted in Fig. 1 and are described in the following section.

Both procedures use a masked transform that contains only parts of the transform within circles of defined radius around each visible diffraction peak. This masked transform is used to calculate a cross-correlation map, which describes the relative translations of the unit cells compared with a reference image. When part of the crystal is used as a reference, the masked transform is back transformed to create a Fourier filtered image (Fig. 1*A*), from which the reference area is selected. This reference area is then used to calculate a map of the cross-correlation function with the filtered image. The height of the cross-correlation peak indicates how well particular areas correlate with the reference area (16).

In this paper, we use an improved reference projection obtained from the best existing low-resolution 3D density map of hR (initially from ref. 12) to unbend the crystal. A new program called MAKETRAN was written, which uses the amplitudes and phases derived from an MTZ file to calculate the Fourier transform of the projection with the same symmetry, magnification, tilt axis/angle, defocus, and astigmatism as the image (Fig. 1*B*). This reference transform is then used to calculate a cross-correlation map with the filtered image. To make the two cross-correlation maps as comparable as possible, the origin for the calculated map transform is set to correspond to the one determined by using the crystal as reference. The unbending procedure using the crystal as reference requires two rounds of unbending, in which the improved reference density from the first pass serves as template for the second. The new

unbending procedure by using a projection of the 3D map as reference required only one pass to reach convergence. However, if the starting 3D density map is very noisy, a second pass by using the improved 3D map of the first round could produce further improvement.

The remaining steps of image processing followed previous methods (12, 16). The crystalline areas are boxed off (BOXIMAGE), and amplitudes and phases were extracted by using MMBOXA. The phases from MMBOXA were corrected for the contrast transfer function because of the defocus and astigmatism. The defocus, tilt axis and angle, and phase origin were then refined in an iterative procedure by using the phase residual between phases from the existing low-resolution 3D map (12) and those extracted from the image transform as criterion for improvement (CTFSEARCH). The steps used to merge the data from all 131 images including scaling of individual image amplitudes to diffraction data of bR, lattice line fitting by least squares, and Fourier calculation of the map were as described previously (12). The anisotropic temperature factors (B_{xy}, B_z) were calculated for all images and used to correct the raw image amplitudes, as described previously (12).

Results

Five of the eighty-five new images were taken in Berlin on Sophie (160 keV) and all others on the 200 kV Hitachi HF 2000 cold FEG microscope. The basic image processing followed the previous procedure (12) with the exception of the correction for the translational distortions of 2D crystals (unbending). Lattice disorder is the major cause of loss of contrast of high-resolution image diffraction spots. Earlier work had shown that these distortions can in part be corrected for by unbending the image by using cross-correlation with a reference area from the center of the crystal to determine the lattice distortions (Fig. 1*A*). This approach is not optimal if the chosen reference area is relatively noisy, disordered, or not representative of the whole crystal.

To carry out the new unbending procedure, a program, MAKETRAN, was used to calculate the reference transform. To remove most of the random nonperiodic noise, the strong spots in the image transform are first masked out, whereas all other parts are set to zero. The radius of the circles around each spot determines the amount of averaging in the filtered image and the extent of remaining noise. If the radius is too small, the filtering causes long range averaging. On the other hand, if the radius is too large, the noise in the filtered image remains high, and a larger reference area is needed. In either case, the correlation map would be unable to follow the finer distortions in the lattice faithfully and would provide a poor description of the unit cell positions.

In practice, the optimal radius of the holes in the mask was determined empirically for each image to find the largest number of good spots defined as having a background-corrected signal-to-noise ratio larger than 1.0 (IQ 1–7, where these IQ numbers refer to a quality index defined as 7× the ratio of background to peak amplitude). Fig. 2 shows the optimization process for image hr3552. The total number of good spots in the 200–3.5 Å range increases with increasing radius to about 32 reciprocal lattice units (614 spots), after which it slowly declines to 575 spots. A good indicator of an improved signal-to-noise ratio is the peak height of the high-resolution image diffraction spots (Fig. 2 *Inset*). In resolution range 4–3 Å, a signal just above background (9 vs. 7, where these IQ numbers refer to a quality index defined as 7× the ratio of background to peak amplitude) is present only when the radius values are between 15 and 35 reciprocal lattice units. The old and new procedures were used to unbend all new images and to reprocess those in Havelka *et al.* (12). In general, radii between 25 and 35 reciprocal lattice units gave the best unbending results.

Fig. 3 compares the total number of good spots extracted for each procedure. The procedures are referred to as unbending by

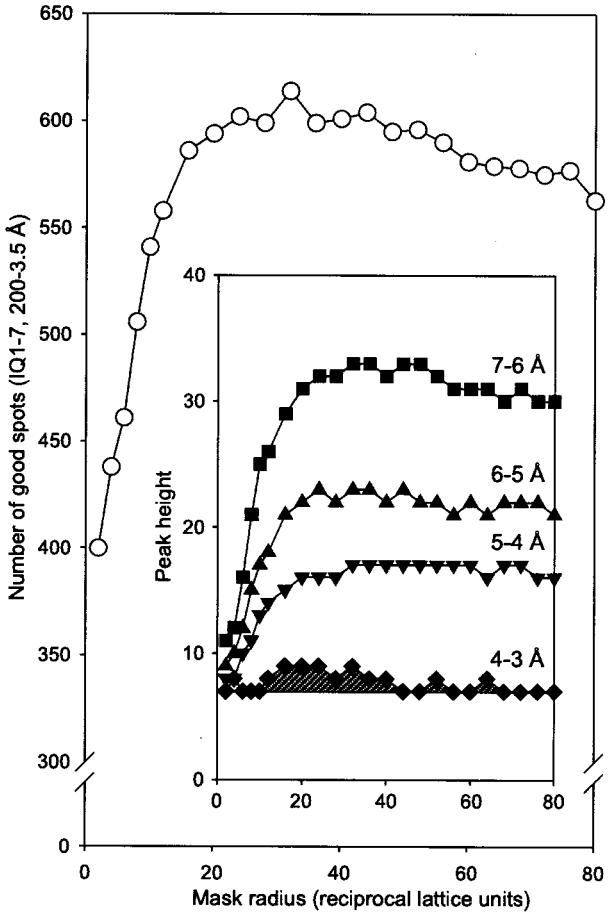

Fig. 2. Optimization of the radius for the mask of the Fourier transform of image 3552. The plot shows the dependence of the final number of good spots obtained in the 200- to 3.5-Å resolution range on the radius used in the reciprocal space averaging procedure. The radius is used to mask the Fourier transform of the image (see *Materials and Methods*). Good spots have a signal-to-noise ratio greater than 1.0 after correction for the background. *Inset* shows for the indicated resolution ranges the relation between the radius and the averaged height of the image diffraction peaks above the perimeter average, scaled so that the average background has a value of 7.

using the "crystal" or the "3D map" as reference. More good spots were extracted when the 3D map was used for unbending than when the crystal was used. On average, the improvement in number of spots was about 8% with the largest being 50%. The best improvements were observed for the poorest images, which were generally those from tilted specimens. In only 4 of 131 images, the unbending by using the 3D map produced a slightly worse result, perhaps because the statistics are derived from a small number of spots or because the input parameters might not be optimally determined.

The net gain because of unbending by using the 3D map consists of an increase by 1,384 spots with signal greater than background (IQ 1–7) that previously had a signal worse than background (IQ 8–9) when the images were unbent by using the crystal as reference (Fig. 3*B*). The results show not only that more reliable spots were extracted, but that the signal-to-background ratio had also increased.

Quality and Resolution of the Dataset. The overall phase residual gives information about the quality of the experimentally determined phases extracted from the transform of the image compared with the phases of the total merged dataset (Fig. 4*A*). The

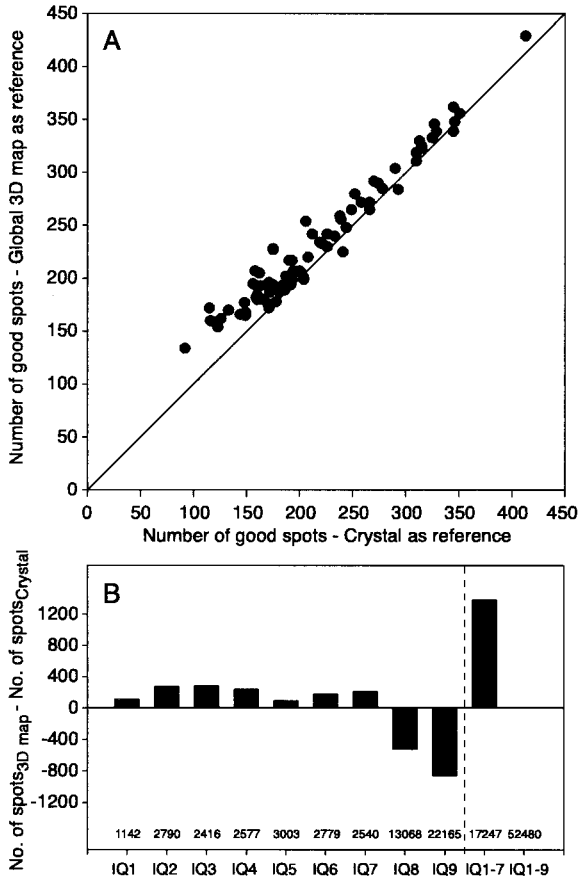

Fig. 3. Number of good spots extracted from the Fourier transform of each image after unbending by using the crystal as reference vs. the 3D density map as reference (*A*) and difference in the total number of spots extracted for the various IQ classes (*B*). Amplitudes and phases were extracted with MMBOXA after unbending of the image by using either the crystal or the 3D density map as reference. The diagonal line indicates no net difference between the number of extracted good spots (IQ 1–7, 200–5.0 Å) after using the two unbending procedures.

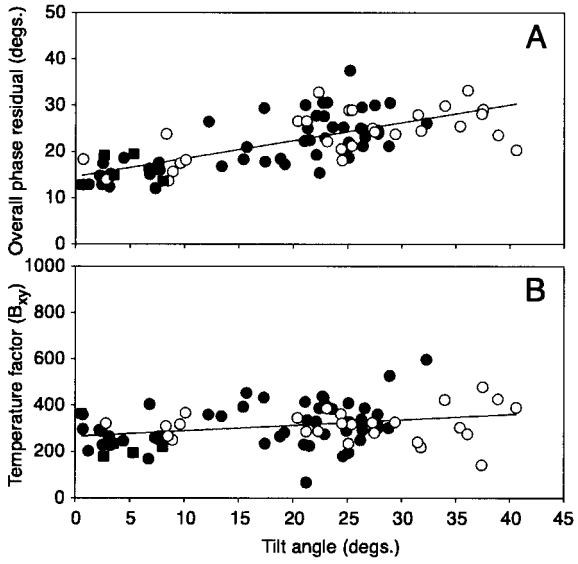

Fig. 4. The overall phase residual (*A*) and the temperature factor B_{xy} (*B*) vs. the tilt angle. The squares represent micrographs taken in Berlin on Sophie (160 keV), whereas the circles indicate images taken on the Hitachi HF2000 in Cambridge. Open symbols are spot-scan exposures, whereas closed ones are flood beam.

phase residual increased with the tilt angle, which is because the structure factors are weaker.

Amplitudes, which fade out with resolution because of image blurring by stage drift, radiation damage, or charging, and lack of flatness and crystalline order of the crystal, can be corrected by application of anisotropic temperature factors, which rescales the amplitudes (Fig. 4*B*) (12). On average, the temperature factor in the plane (B_{xy}) was 311 ± 86. A slight overall increase in temperature factor in the plane of the membrane with increasing tilt angle was found, which may indicate further scope for improvement (Fig. 4*B*). The temperature factor perpendicular to the membrane (B_z) had an average value of 690 ± 404, probably because of lack of flatness and vertical movement of the specimen during imaging.

To estimate the resolution, the dataset was divided into halves and the resulting phases compared as function of resolution. A set of random phases would give a phase residual of 90°. The average phase residual in resolution shells was as follows: 100.0–9.0 Å, 24.4°; 9.8–7.0, Å 35.9°; 7.0–5.7 Å, 54.5°; 5.7–4.9 Å, 64.8°, and 4.9–4.0 Å, 79.9°. Thus, the projection phases were reliable to 5 Å with some significant data beyond. The overall effective resolution could be calculated from the point-response function. The dataset compared well to a simulated 5-Å dataset with tilt limited to 35° and 85% completeness. The resolution perpendicular to the membrane was calculated to be 12 Å.

Description of the Electron Density Map of hR. All seven helices are now well resolved and their positions accurately determined. When an atomic model of bR is refined as a rigid body into the electron density map of hR, all helices have continuous density. From the high primary sequence identity and hydropathy profiling, the length of the helices of bR and hR must be very similar. Most loops of the two membrane proteins are also comparable in length except for the N terminus and BC loop, which are 20 and 6 aa residues longer in hR, respectively. With the improved resolution perpendicular to the membrane, the density representing the vertical extension of the helices now agrees well with bR, but the loops are still not well enough resolved to be traced. There is density for the β-ionone ring of the retinal, as can be seen in Fig. 5 *A* and *D*. Because of the poorer resolution perpendicular to the membrane, the density has an elongated shape and is partly fused with helix E (Fig. 5*D*).

Sixteen amino acids that line the intramolecular transmembrane space around the retinal are conserved in all members of the archeal rhodopsin family (1), and several tryptophans surround the polyene chain of the retinal. When the electron density surrounding the retinal binding pocket is inspected, three density bulges can be seen, which correspond to the approximate positions of hR-tryptophans Trp-112, Trp-207, and Trp-214.

Discussion

Many membrane proteins of medical or biological importance are difficult to overexpress, and only small quantities of functional protein can be obtained in pure solubilized form. In addition, many of these proteins are unstable in detergent, and large well-ordered crystals, either 2D or 3D, may be difficult to obtain. hR crystals are ideal specimens to test improvements in methods of computer-based image analysis, because the resulting density should be very similar to that for the homologous bR. In this paper, we report a major improvement of the resolution of the 3D structure of hR compared with that of the previous map (12). Two methodological advances have allowed us to

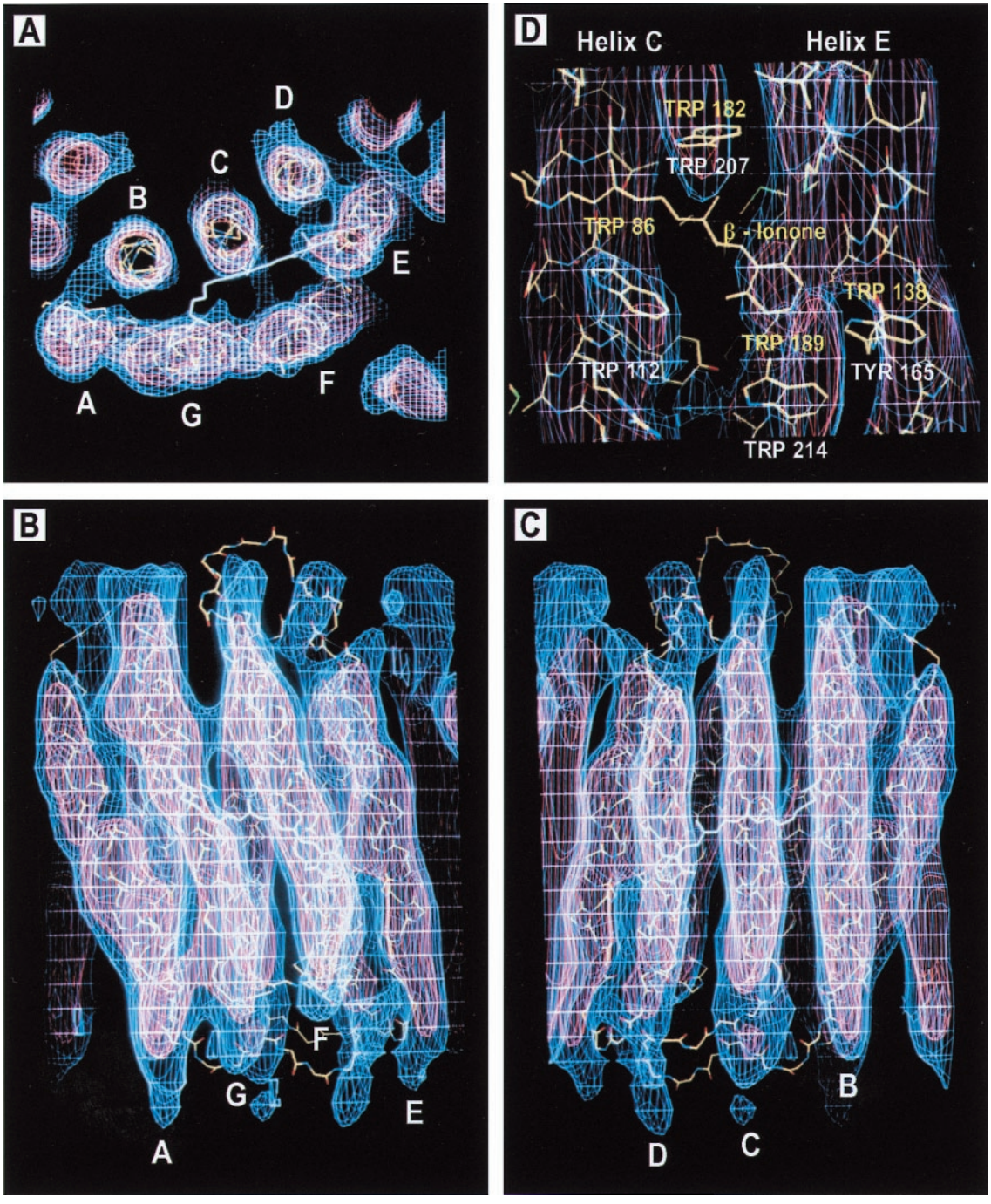

Fig. 5. Overviews of the electron density map of hR at 6.5 Å (*A–C*) and 5.5 Å (*D*). The electron density map of the hR molecule as viewed from the cytoplasmic side (*A*), toward the tilted helices A, G, F, and E (*B*), and toward the virtually untilted helices D, C, and B (*C*) (*Left* to *Right*). Also shown is a closeup of the retinal-binding pocket as viewed toward helices C and E (helix D is not visible). The atomic model of bR (17) was rigid-body refined to the density by using the RSR_Rigid routine of the program O (18). *A–C* show the peptide backbone and the retinal chromophore of bR in the density of hR, and *D* also shows the side chains. The tryptophan residues of bR and the β-ionone ring of the retinal are labeled in yellow and the densities of equivalent hR residues in white. One of the two methyl groups at position 5 of the β-ionone ring is occluded by the other. The contours are at 16% (blue) and at 32% (orange) of the maximum density peak height.

achieve the higher resolution. The first is the addition of many new images taken on FEG microscopes. On average twice as many good spots per image (IQ 1–7, 200–6.5 Å) were obtained from these images compared with non-FEG images (170 vs. 86 spots). Furthermore, the average temperature factor (B_{xy}) parallel to the membrane plane, which needed to be applied [i.e., $\exp(B/4d^2)$] to restore the weak power of the high-resolution amplitudes, was 310 in this study (490 previously) (12). Because the crystals are the same in size and order as in the previous study, the improvement is because of better microscopy, better coherence of the electron beam, and less ice contamination.

The second reason for improvement of the data is the improved unbending procedure, which leads to more accurate corrections of translational disorders. In this paper, we have used

the amplitudes and phases of the existing structure as reference, but in principle, any appropriate 3D density from a homologous protein could be used (e.g., bR) to create an hR-like crystal by using the $p42_12$ symmetry. Provided the reference density was calculated to exclude high-resolution terms, it would not introduce bias toward the reference structure, and statistical tests could be used to prove that the new structure contained significant new features. A prerequisite for a successful use of any global reference structure is the accurate determination of the values for magnification, cell parameters, tilt axis/angle, defocus, and astigmatism to generate an appropriate reference that mimics the properties of the image under study.

The resolution is much improved from the previous 7 Å in the plane and 20 Å perpendicular (12) to 5 Å in the plane and 12 Å perpendicular. At this resolution, hR and bR are virtually indistinguishable. The helix positions between bR and hR are now essentially the same within experimental error. In the retinal binding pocket, density bulges can be found that indicate the approximate position of the tryptophan cluster and the β-ionone ring of the retinal.

So why have we not achieved atomic resolution? The total number of hR molecules that went into the Fourier calculations for this structure is estimated to be about one million. This is less than the 5 million and 2.6 million that went into the bR and light-harvesting complex II, respectively (16, 19–20), but not sufficiently less to make such a difference to the resolution attained. The key problem is the fading with resolution of the amplitude of the Fourier components of the image and the resultant drop in signal-to-noise ratio and its resulting effect on phase error. The weak electron diffraction patterns that could be taken from the small hR crystals showed weak spots that faded out at 5 Å (11). Some reliable phases are present in the data described here out to 4 Å, but not beyond. Further improvement of the resolution of the structure beyond 5 Å would therefore have to come from an improvement of the size and intrinsic order of the crystals, either by recrystallization from detergent-solubilized hR or by fusion of crystalline patches. In addition, it might be possible to improve the flatness of the specimen by embedding the crystals in glucose, tannin, or trehalose as was done for 2D crystals of bR, light-harvesting complex II, aquaporin, and tubulin (20–23), rather than in ice as has been done here.

In principle, a good-quality electron micrograph of a membrane protein sample should contain atomic resolution pictures of the molecules whether they are arranged into a perfect 2D lattice or a disordered 2D lattice or exist as completely independent individual molecules solubilized in detergent. The difference lies in the effort required to extract the information and the signal-to-noise ratio of the resulting average structure. Perfect crystals require little more than accurate knowledge of the 2D crystal lattice parameters so that averaging molecules whose position in the crystal is predetermined is done accurately. By comparison, work on single particles requires the accurate determination of the position and orientation of each particle, a requirement that is increasingly difficult to meet as the size of the particle gets smaller (20). At present, although some preliminary experiments by using pictures of crystals (24) indicate that single-molecule microscopy of molecules or molecular assemblies as small as 100 kDa (such as the hR tetramer or the bR trimer) at atomic resolution may become possible, we have not yet reached that stage. The procedure described in the current paper is an extension of the perfect 2D crystal approach into the middle ground represented by disordered crystals. This procedure is still based on an unbending procedure and so it tries to turn a poorly ordered crystal into a more perfect crystal by using the best possible reference structure to describe the lattice distortions. However, because of limited signal-to-noise ratio for individual hR tetramers at present, it is still better to make use of the imperfect crystalline order to constrain the unbending than to treat each hR tetramer as a fully independent entity. In future, it should be possible to improve the pictures and the computing procedures so that the structure of molecules forming poorly ordered crystals or no crystals at all can be determined at resolutions sufficient to build an atomic model correctly.

We thank Fritz Zemlin and colleagues for the five pictures taken in Berlin. John Berriman, Pat Edwards, Peter Rosenthal, and Gebhard Schertler are acknowledged for their help with the electron microscopy and Joyce Baldwin for calculations of the point spread function. E.K. is the recipient of a European Molecular Biology Organisation long-term fellowship and was supported by a grant from the European Union (BIO4-CT-972119).

1. Mukohata, Y., Ihara, K., Tamura, T. & Sugiyama, Y. (1999) *J. Biochem.* **125,** 649–657.
2. Stoeckenius, W. (1999) *Protein Sci.* **8,** 447–459.
3. Spudich, J. L. (1998) *Mol. Microbiol.* **28(6),** 1051–1058.
4. Dér, A., Száraz, S., Tóth-Boconádi, R., Tokaji, Zs., Keszthelyi, L. & Stoeckenius, W. (1991) *Proc. Natl. Acad. Sci. USA* **88,** 4751–4755.
5. Marti, T., Otto, H., Rösselet, S. J., Heyn, M. P. & Khorana, H. G. (1992) *J. Biol. Chem.* **267,** 16922–16927.
6. Sasaki, J., Brown, L. S., Chon, Y.-S., Kandori, H., Maeda, A., Needleman, R. & Lanyi, J. K. (1995) *Science* **269,** 73–75.
7. Tittor, J., Haupts, U., Haupts, C., Oesterhelt, D., Becker, A. & Bamberg, E. (1997) *J. Mol. Biol.* **271,** 405–416.
8. Bamberg, E., Tittor, J. & Oesterhelt, D. (1993) *Proc. Natl. Acad. Sci. USA* **90,** 639–643.
9. Váro, G., Brown, L. S., Needleman, R. & Lanyi, J. (1996) *Biochemistry* **35,** 6604–6611.
10. Subramaniam, S. (1999) *Curr. Opinion Struct. Biol.* **9,** 462–468.
11. Havelka, W. A., Henderson, R., Heymann, J. A. W. & Oesterhelt, D. (1993) *J. Mol. Biol.* **234,** 837–846.
12. Havelka, W. A., Henderson, R. & Oesterhelt, D. (1995) *J. Mol. Biol.* **247,** 726–738.
13. Heymann, J. A., Havelka W. A. & Oesterhelt, D. (1993) *Mol. Microbiol.* **7(4),** 623–630.
14. Bullough, P. A. & Henderson, R. (1987) *Ultramicroscopy* **21,** 223–230.
15. Crowther, R. A., Henderson, R. & Smith, J. M. (1996) *J. Struct. Biol.* **116,** 9–16.
16. Henderson, R., Baldwin, J. M., Ceska, T. A., Zemlin, F., Beckmann, E. & Downing, K. H. (1990) *J. Mol. Biol.* **213,** 899–929.
17. Grigorieff, N., Ceska, T. A., Downing, K. H., Baldwin, J. M. & Henderson, R. (1996) *J. Mol. Biol.* **259(3),** 393–421.
18. Jones, T. A., Zou, J. Y., Cowan, S. W. & Kjeldgaard, M. (1991) *Acta Crystallogr. A* **47,** 110–119.
19. Kühlbrandt, W., Wang, D. N. & Fujijoshi, Y. (1994) *Nature (London)* **367,** 614–621.
20. Henderson, R. (1995) *Q. Rev. Biophys.* **28,** 171–193.
21. Wang, D. N. & Kühlbrandt, W. (1991) *J. Mol. Biol.* **217,** 691–699.
22. Waltz, T., Hirai, T., Murata, K., Heymann, J. B., Mitsuoka, K., Fujiyoshi, Y., Smith, B. L., Agre, P. & Engel, A. (1997) *Nature (London)* **387,** 624–627.
23. Nogales, E., Wolf, S. G. & Downing, K. H. (1998) *Nature (London)* **391,** 199–203.
24. Grigorieff, N., Beckmann, E. & Zemlin, F. (1995) *J. Mol. Biol.* **254(30),** 404–415.